NJC

Accepted Manuscript

This is an *Accepted Manuscript*, which has been through the Royal Society of Chemistry peer review process and has been accepted for publication.

Accepted Manuscripts are published online shortly after acceptance, before technical editing, formatting and proof reading. Using this free service, authors can make their results available to the community, in citable form, before we publish the edited article. We will replace this *Accepted Manuscript* with the edited and formatted *Advance Article* as soon as it is available.

You can find more information about *Accepted Manuscripts* in the Information for Authors.

Please note that technical editing may introduce minor changes to the text and/or graphics, which may alter content. The journal's standard Terms & Conditions and the Ethical guidelines still apply. In no event shall the Royal Society of Chemistry be held responsible for any errors or omissions in this *Accepted Manuscript* or any consequences arising from the use of any information it contains.

ROYAL SOCIETY OF CHEMISTRY

www.rsc.org/njc

Cite this: DOI: 10.1039/c0xx00000x

www.rsc.org/xxxxxx

ARTICLE TYPE

Promising ceria-samaria based nano-oxides for low temperature soot oxidation: A combined study of structure-activity properties

Putla Sudarsanam, Kuncham Kuntaiah and Benjaram M. Reddy*

Received (in XXX, XXX) Xth XXXXXXXXX 20XX, Accepted Xth XXXXXXXXX 20XX

DOI: 10.1039/b000000x

Design of promising heterogeneous catalysts is an urgent task for protecting environment from automotive exhaust pollutants. In this work, the catalytic efficiency of nanosized Ce-Sm and Ce-Sm/γ-Al_2O_3 samples synthesized by economical coprecipitation and deposition coprecipitation methods, respectively, was investigated for diesel soot oxidation. The physicochemical properties of the synthesized materials were systematically analyzed by means of XRD, BET surface area, Raman, TG-DTA, FT-IR, HRTEM, ICP-OES, XPS, and UV-vis DRS techniques. XRD studies confirmed the formation of nanocrystalline single phase Ce-Sm-oxide solid solutions. HRTEM images showed the presence of smaller sized nanocrystals (~4-15 nm) in the synthesized samples. The Ce-Sm/γ-Al_2O_3 sample exhibited remarkable thermal stability compared with Ce-Sm-oxide and CeO_2 samples as evidenced by an insignificant variation in the crystallite size and BET surface area against high thermal treatments. Owing to disparity in the oxidation state of Sm^{3+} and Ce^{4+}, abundant oxygen vacancies were formed in both Ce-Sm and Ce-Sm/γ-Al_2O_3 samples. Interestingly, the oxygen vacancy concentration was substantially decreased with the increase of calcination temperature attributed to well ordering level of the samples. Catalytic activity results revealed that both Ce-Sm and Ce-Sm/γ-Al_2O_3 samples show excellent soot oxidation performance compared with pristine CeO_2 due to the presence of abundant oxygen vacancies and superior BET surface area. A 50% soot conversion was achieved at ~690, 697, and 835 K with Ce-Sm, Ce-Sm/γ-Al_2O_3 and CeO_2 samples calcined at 773 K, respectively. It was found that the soot oxidation efficiency of Ce-Sm and Ce-Sm/γ-Al_2O_3 samples strongly depends on the calcination temperature. Despite its trivial activity difference with respect to Ce-Sm sample, the outstanding thermal stability of the Ce-Sm/γ-Al_2O_3 sample is vital in view of the practical working conditions of the diesel engines.

1. Introduction

Nowadays, the environment protection from harmful automotive exhaust emissions represents a great challenge to the scientific community. Particularly, soot particles released from diesel vehicles are the most detrimental pollutants that cause serious health problems, including respiratory, mutagenic, and cardiovascular diseases.[1-3] Soot particles further assist the accumulation of NO_x pollutants into the atmosphere by inhibiting the activity of post-treatment catalysts.[3] Owing to high surface area and pore volume, other environment pollutants also adsorb on the soot particles and make them more hazardous.[4] Hence, many studies have been performed for the abatement of soot particles. The combination of diesel particulate filters (DPFs) with catalytic materials is found to be an efficient solution for the soot combustion.[5,6] The key function of DPFs is to capture the soot particles present in the engine emissions, thus preventing their release into the atmosphere.[1] The collected soot particles are continuously oxidized by catalytic materials to enable self-regeneration of DPFs. Many types of catalysts have been studied for the soot oxidation.[7,8] Amongst, noble metal based catalysts exhibit remarkable soot oxidation activity.[9,10] However, noble metals are expensive and emit large amounts of hazardous sulfates (e.g., Pt).[9] In addition, the thermal stability of the catalysts is a crucial factor because the temperature inside the DPFs increase enormously due to high exothermic soot combustion process, which eventually leads to deactivation of the catalysts.[11] The development of high efficient and thermally stable catalysts without noble metals is therefore an issue of ongoing investigations in the field of diesel soot oxidation.[8]

As one of the potential alternative noble metal based catalysts, ceria (CeO_2) has attracted much attention due to its unique structural and redox properties.[12,13] Especially, the facile Ce^{4+}/Ce^{3+} redox cycle confers the ability of cerium to form active oxygen species on the catalyst surface, which play a favourable role in the soot oxidation. It is reported that the commercially available PSA (Peugeot-Citroën Societéd Anonyme) system uses a cerium-fuel additive to decrease the ignition temperature of soot.[11] The regeneration of DPFs can also be improved by the addition of nano-CeO_2 to the DPF.[11] Besides, CeO_2 is a key component in several industrial processes, including three-way-catalysis (TWC), fluid-cracking catalysis, waste water treatment, water-gas-shift reaction, solar thermochemical hydrogen generation, solid oxide fuel cells, etc.[14-17] Despite its widespread applications, the use of pure CeO_2 in heterogeneous catalytic

Inorganic and Physical Chemistry Division, CSIR – Indian Institute of Chemical Technology, Uppal Road, Hyderabad – 500 007, India.
E-mail: bmreddy@iict.res.in; mreddyb@yahoo.com; Fax: +91 40 2716 0921; Tel.: +91 40 2719 3510.

†Electronic supplementary information (ESI) available: TG-DTA, FT-IR and XPS studies of synthesized samples.

reactions is still limited due to its poor thermal stability.[7] At elevated temperatures, the ceria particles undergo easy sintering, resulting in unfavourable structural changes and thereby, decreased catalytic performance.

Incorporation of suitable metal ions into the CeO_2 lattice is known to be a versatile way to overcome the thermally induced negative effects.[18,19] Particularly, metal ions having similar ionic radius and electronegativity to those of Ce are considered to be indispensable to develop promising CeO_2-based solid solutions.[20,21] Samarium (Sm) is one of the potential dopants to improve the structural and chemical properties of ceria because of its resemblance in the ionic radius and electronegativity with respect to the Ce.[22] Additionally, owing to the difference in the oxidation states of Ce^{4+} and Sm^{3+}, large amounts of oxygen vacancies can be formed through charge compensation mechanism. For instance, substitution of Ce^{4+} by Sm^{3+} is accompanied by creation of an oxygen vacancy for every two Sm^{3+} cations to balance the charge in the CeO_2 lattice. Therefore, the efficiency of Ce-Sm-oxide materials have been studied for a number of catalytic applications, such as HCl oxidation, Deacon reaction, CO oxidation, solid oxide fuel cells, reforming of methanol, allylic oxidation of cyclohexene, oxidation of benzyl alcohol, etc.[19,23-26] Efforts to further enhance the desired properties of Ce-based solid solutions have also been made by dispersing them over a thermally stable and high surface area support material.[27] Transition Al_2O_3 is one of the commonly used supports for catalytically active phases because of its remarkable textural properties. Hence, it can be expected that the addition of Al_2O_3 to the Ce-Sm-oxide solid solution improves its thermal stability as well as its structure-activity properties.

The present work was undertaken with an aim to develop high efficient CeO_2-based solid solutions for diesel soot oxidation. Accordingly, Al_2O_3 supported CeO_2-Sm_2O_3 and unsupported CeO_2-Sm_2O_3 solid solutions were prepared by deposition-coprecipitation and coprecipitation methods, respectively. The synthesized samples were calcined at different temperatures (from 773 to 1073 K) to understand their thermal stability, which is vital for the application of these materials in an actual soot trap. The physicochemical properties of the synthesized samples were deeply investigated by employing different characterization techniques, namely, thermogravimetric differential thermal analysis (TG-DTA), X-ray diffraction (XRD), BET surface area, high resolution transmission electron microscopy (HRTEM), inductively coupled plasma optical emission spectrometry (ICP-OES), Raman spectroscopy, Fourier transform infrared (FTIR) spectroscopy, UV-visible diffuse reflectance spectroscopy (UV-vis DRS), and X-ray photoelectron spectroscopy (XPS). The catalytic efficiency of the Ce-Sm and Ce-Sm/Al_2O_3 samples was evaluated for diesel soot oxidation. Many attempts have been made to correlate the structural features of the synthesized materials with their catalytic soot oxidation efficiency.

2. Experimental section

2.1 Catalyst Preparation

The CeO_2-Sm_2O_3 solid solution with an optimized CeO_2:Sm_2O_3 (CS) = 80:20 (molar ratio based on metal oxides) was synthesized by a facile coprecipitation method from ultra-high dilute aqueous solutions. In a typical procedure, the required quantities of $Ce(NO_3)_3{\cdot}6H_2O$ [99.99%, Aldrich] and $Sm(NO_3)_3{\cdot}6H_2O$ [99.9%, Aldrich] were dissolved in 2L of double distilled water separately and mixed together under mild stirring conditions. The stirring was continued (approximately for 1 h) until the formation of a clear solution. Afterward, an aqueous NH_3 solution was added slowly (min. 2 h duration) to the above mixture solution until the pH of the solution reached to ~9.5. The obtained precipitates were decanted, filtered off, and washed with double distilled water multiple times to remove the weakly adhered ions (e.g., nitrates) on the sample surface followed by oven drying at 393 K for 12 h. The oven dried sample was crushed using an agate mortar and calcined at 773 K for 5 h at a heating rate of 5 K min^{-1} in dry air. Finally, some portions of the finished catalyst were further calcined at 1073 K for 5 h in dry air using the same heating ramp to examine the thermal behaviour of the CeO_2-Sm_2O_3 sample.

The Al_2O_3-supported CeO_2-Sm_2O_3 solid solution with CeO_2:Sm_2O_3:Al_2O_3 (CSA) = 80:20:100 (molar ratio based on metal oxides) was prepared by a deposition coprecipitation method. In brief, the desired amount of finely powdered γ-Al_2O_3 (Harshaw, BET surface area 208 m^2 g^{-1}) was first dispersed in about 3500 mL of deionized water and stirred for 2 h. The required amounts of Ce and Sm precursors were dissolved separately in deionized water and mixed together followed by the addition of support suspension to it. Subsequently, an aq. NH_3 solution was added drop wise to the mixture solution until the reach of an appropriate pH of the solution (~9.5). The resulting slurry was filtered off, washed with deionized water, oven-dried at 393 K for 12 h, and subsequently calcined at 773 K for 5 h at a heating rate of 5 K min^{-1} in dry air. Finally, some portions of the finished catalyst were further heated at different temperatures for 5 h using the same heating ramp to monitor thermal stability. For comparison, pure CeO_2 (C) was also prepared following the same procedure under identical conditions.

2.2. Catalyst Characterization

XRD studies were performed on a Rigaku diffractometer using Cu Kα radiation (0.1540 nm), operated at 40 kV and 40 mA. The diffractograms were recorded in the 2θ range of 3-80º with a 2θ step size of 0.02º and a step time of 2.4 s. The XRD phases present in the samples were identified with the help of a Powder Diffraction File-International Center for Diffraction Data (PDF-ICDD). The average crystallite size of the samples were estimated using Scherrer equation from line broadening and the lattice parameter was calculated by a standard cubic indexation method using the intensity of the most prominent peak (111).

Specific surface area of the synthesized materials was measured by N_2 adsorption on a Micromeritics Gemini 2360 instrument. Prior to analysis, the samples were oven-dried at 393 K for 12 h and flushed with Argon gas for 2 h to remove any surface adsorbed residues. Surface area was calculated by utilizing the desorption data. TG-DTA analysis was performed on a Mettler Toledo TG-SDTA instrument. The samples were heated from ambient temperature to 1073 K under the flow of N_2. The heating rate in each case was kept at 10 K/min.

Raman spectra were recorded with a Horiba Jobin-Yvon HR800 Raman spectrometer equipped with a liquid-nitrogen cooled charge coupled device (CCD) detector and a confocal microscope. The emission line at 638-nm from Ar^+ laser (Spectra Physics) was focused on the sample under the microscope with the diameter of the analyzed spot being ~1 μm, under the ambient conditions. The time of acquisition was adjusted according to the intensity of Raman scattering. The wavenumber values reported from the spectra are accurate to within 2 cm^{-1}. The FTIR spectra were recorded on a Nicolet 740 FT-IR spectrometer at ambient conditions using KBr discs with a nominal resolution of 4 cm^{-1} and averaging 100 spectra. The elemental analysis of the samples was performed using ICP-OES technique (Thermo Jarrel Ash model IRIS Intrepid II XDL, USA) following sample dissolution by acid digestion method.

UV-vis DRS measurements were performed over the wavelength range of 200-750 nm using a GBS-Cintra 10e UV-vis NIR spectrophotometer with an integration sphere diffuse reflectance attachment. Sample was diluted in a $BaSO_4$ matrix by pelletization. HRTEM studies were made on a JEOL JEM-2100F instrument equipped with a slow-scan CCD camera and the accelerating voltage of the electron beam was 200 kV. The preparation of samples for HRTEM analysis involved sonication of sample in ethanol for 2-5 min, followed by deposition of a drop on the copper grid supporting a perforated carbon film and allowed to dry. The specimen was examined under vacuum at room temperature. XPS measurements were carried out on a PHI 5400 instrument with a 200 W Mg Kα probe beam. The analysis was done at room temperature and pressures were typically in the order of less than 10^{-8} Pa. The spectrometer was configured to operate at high resolution with a passing energy of 100 eV. Prior to the analysis, the samples were evacuated at high vacuum and then introduced into the analysis chamber. Survey and multi-region spectra were recorded at C 1s photoelectron peaks.

2.3. Activity Measurements

The catalytic efficacy of the samples for soot oxidation was studied in a thermogravimetric analyzer (Mettler Toledo, TGA/SDTA851e). Oxidation experiments consisted of heating the catalyst-soot mixtures at 10 K min^{-1} from RT to 1273 K in a 100 ml min^{-1} flow of oxygen. These experiments were conducted in 4–5 cycles using the same catalyst sample and no appreciable change in the soot oxidation activity was noticed. The activity measurements were performed in 'tight contact' (ground in an agate mortar) condition with catalyst-soot mixtures in 4:1 wt/wt ratio. The model soot used in the present study is Printex-U provided by Degussa. This soot was proven to be an appropriate model for the soot oxidation reaction.

3. Results and discussion

3.1 Synthesis and characterization of CeO_2, Ce-Sm and Ce-Sm/Al_2O_3 catalysts

The Ce-Sm and Ce-Sm/Al_2O_3 catalysts along with pure CeO_2 were synthesized using precipitation procedures with aq. NH_3 solution as the precipitating agent. The samples were thoroughly washed with double distilled water to remove the impurities from the sample surface. The synthesized samples were treated at different temperatures ranging from 773 to 1073 K for 5 h in air. The physicochemical characterization of the catalysts has been undertaken using a number of spectroscopic and non-spectroscopic techniques.

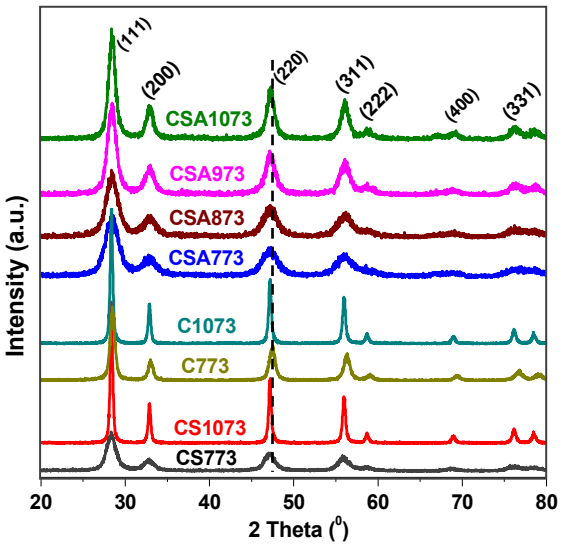

Fig. 1 Powder X-ray diffraction patterns of pure CeO_2 (C), CeO_2-Sm_2O_3 (CS), and CeO_2-Sm_2O_3/Al_2O_3 (CSA) samples calcined at different temperatures.

The XRD patterns of CeO_2, Ce-Sm, and Ce-Sm/Al_2O_3 samples are presented in Fig. 1. It was obvious from Fig. 1 that all samples show typical XRD peaks at 2θ = (111), (200), (220), (311), (222), (400), and (331), indicating fluorite structured CeO_2.[28,29] Interestingly, no XRD peaks due to Sm-oxide phases are found for Ce-Sm and Ce-Sm/Al_2O_3 samples. This observation reveals incorporation of Sm into the CeO_2 lattice. The increased lattice parameters of Ce-Sm and Ce-Sm/Al_2O_3 samples compared with that of pure CeO_2 also evidence the above observation (Table 1). The variation in the lattice parameters is due to difference in the ionic radii of the Sm^{3+}-dopant (1.08 Å) and Ce^{4+}-host (0.97 Å). The lattice parameters of pure CeO_2, Ce-Sm, and Ce-Sm/Al_2O_3 samples calcined at 773 K were found to be ~0.541, 0.545, and 0.544 nm, respectively. Usually, γ-Al_2O_3 shows XRD peaks at 2θ = 37.2, 45.8 and 67.0°.[30] In the present work, only one weak peak at 2θ = 67° is observed for Ce-Sm/Al_2O_3 sample calcined at 1073 K, which indicates presence of γ-Al_2O_3. Although other XRD peaks related to γ-Al_2O_3 are not observed, we can't exclude the overlapping of Al_2O_3 peak at 45.8° with the CeO_2 (220) peak as well as low intensity of the XRD peak at 37.2° in the CSA1073 sample. On the other hand, no XRD peaks related to γ-Al_2O_3 phase were found for the CSA sample calcined at 773, 873, and 973 K, which indicates amorphous nature of Al_2O_3.[31] It is therefore suggested that the crystallization of Al_2O_3 to give XRD peaks strongly depends on the calcination temperature.[32] As well, no XRD peaks corresponding to Ce-Al mixed oxides were found for all CSA samples. It is difficult for Al^{3+} ions to incorporate into the CeO_2 lattice since the pre-calcined Al_2O_3 fine powders were used as the precursors in the present study.[30] If $Al(NO_3)_3 \cdot 9H_2O$ is used as Al precursor, there is a huge possibility for the formation of Al^{3+}-doped CeO_2 solid solution through simultaneous coprecipitation

of Al and Ce precursors.[33,34] As per the literature, the $CeAlO_3$ mixed oxides could be formed at high calcination temperatures.[35] It is therefore suggested that the formation of Ce-Al mixed oxides strongly depends on the preparation method adopted and the calcination conditions employed.

Interestingly, the intensity of the diffraction peaks of Ce-Sm and Ce-Sm/Al_2O_3 samples was considerably decreased along with the enhancement of peak width with respect to CeO_2. These observations clearly reveal the formation of smaller sized crystallites in the Ce-Sm and Ce-Sm/Al_2O_3 samples. To understand this, the average crystallite sizes of CeO_2, Ce-Sm, and Ce-Sm/Al_2O_3 samples were estimated by means of Scherrer equation and the obtained values are summarized in Table 1. As can be observed, the crystallite size of CeO_2 was dramatically decreased after the addition of dopant (Sm) and support (Al_2O_3) to it. Amongst, the decrease in the crystallite size is more for the Ce-Sm/Al_2O_3 sample. The determined average crystallite sizes of 773 K calcined CeO_2, Ce-Sm, and Ce-Sm/Al_2O_3 samples are ~8.9, 7.6, and 5.4 nm, respectively. In contrast, the intensity of the XRD peaks was increased for all samples at higher calcination temperatures. This observation suggests the formation of large sized crystallites caused by thermal sintering at elevated conditions. To our surprise, very slight increase in the crystallite size of Ce-Sm/Al_2O_3 sample is noticed with the increase of calcination temperature compared with Ce-Sm and pure CeO_2 samples. This remarkable result indicates a favourable role of the Al_2O_3 support towards inhibition of CeO_2 crystal growth against higher thermal treatments, which is a significant observation in the present work. The obtained average crystallite sizes of CeO_2, Ce-Sm, and Ce-Sm/Al_2O_3 samples calcined at 1073 K are ~32.5, 25.1, and 9.5 nm, respectively. Compared with pure CeO_2, a slight shift in the XRD patterns of Ce-Sm and Ce-Sm/Al_2O_3 samples was observed (evidence from lattice parameter values, Table 1) with the increase of calcination temperature, which signifies the occurrence of the some compositional changes along with crystallite growth.[12]

Table 1 BET surface area (BET SA), crystallite size (D), and lattice parameter (LP) of pure CeO_2 (C), Ce-Sm (CS), and Ce-Sm/Al_2O_3 (CSA) samples calcined at different temperatures

Sample	BET SA (m^2g^{-1})	D (nm)[a]	LP (nm)[a]
C773	41	8.9	0.541
C1073	8	32.5	0.541
CS773	84	7.6	0.545
CS1073	55	25.1	0.543
CSA773	132	5.4	0.544
CSA873	120	5.7	0.546
CSA973	110	7.3	0.540
CSA1073	98	9.5	0.541

[a] From XRD studies.

A major goal in heterogeneous catalysis is to develop potential catalytic materials with superior surface area because the performance of a catalyst is strongly related to its specific surface area.[36] Although the fluorite structure of CeO_2 is preserved at high thermal treatments, its catalytic efficiency might be decreased due to loss of the surface area caused by thermal sintering.[37] Hence, understanding the variation of CeO_2 surface area by increasing the calcination temperature is vital to prepare promising Ce-based solid solutions. Table 1 shows the specific surface areas of the CeO_2, Ce-Sm, and Ce-Sm/Al_2O_3 samples calcined at different temperatures. It is clear from Table 1 that both dopant and support show a beneficial effect on the improvement of specific surface area of CeO_2. The obtained specific surface areas of CeO_2, Ce-Sm, and Ce-Sm/Al_2O_3 samples calcined at 773 K are 41, 84, and 132 m^2/g, respectively. In general, the decrease of particle size results in improved surface area of the materials. Therefore, the observed superior surface area of the Ce-Sm/Al_2O_3 sample is most probably due to its smaller crystallite size (Table 1). With the increase of calcination temperature from 773 to 1073 K, the specific surface area of the CeO_2 was drastically decreased from 41 to 8 m^2/g. Conversely, an insignificant decrease in the specific surface area of Ce-Sm and Ce-Sm/Al_2O_3 samples was noticed with the increase of calcination temperature. Surprisingly, even at higher thermal treatments, the Ce-Sm/Al_2O_3 sample showed superior BET surface area compared with Ce-Sm sample. The specific surface area of 1073 K calcined Ce-Sm and Ce-Sm/Al_2O_3 samples were found to be ~55 and 98 m^2/g, respectively. It is therefore suggested that the addition of support (Al_2O_3) not only improves the surface area of the CeO_2, but also preserves its surface area against higher thermal treatments.

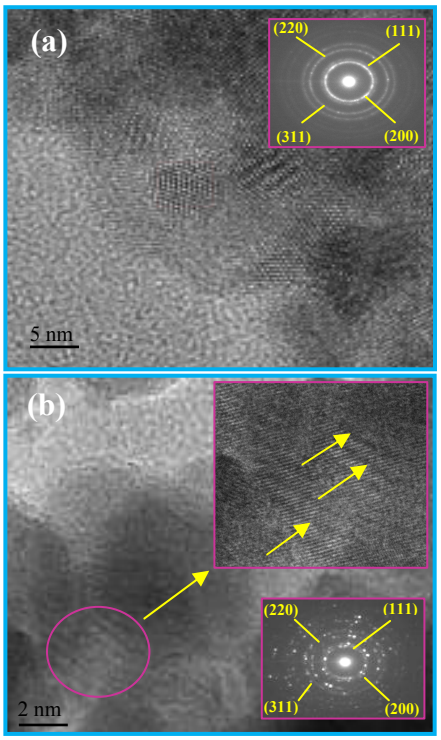

Fig. 2 HRTEM images and the corresponding selected-area electron diffraction (SAED) pattern of CeO_2-Sm_2O_3 (CS) sample calcined at (a) 773 K and (b) 1073 K.

HRTEM analysis was performed to explore the structural evolution of synthesized samples at atomic scale. The HRTEM micrographs of Ce-Sm and Ce-Sm/Al_2O_3 samples are shown in Figs. 2 and 3, respectively. It can be noted that all samples are well crystalline and seems to be octahedral in shape.[38] Nonetheless, it is very difficult to exactly estimate the terminating surfaces of a crystal by HRTEM analysis due to the fact that the image is a 2-dimensional projection of a 3-dimensional object. A geometrical model is necessary for confirming the terminating surfaces of a crystal. On the other hand, the selected area electron diffraction patterns of all samples reveal the cubic structured ceria with (111), (200), (220), and (311) planes, supporting the observations made from the XRD studies. A closer examination of Figs. 2a and 3a reveal the presence of smaller sized crystallites in the range of ~4-8 nm. With the increase of calcination temperature from 773 to 1073 K, the size of particle measured by this technique increases from ~4-8 to 12-15 nm (Figs. 2b and 3b), respectively. These measurements were performed only on few particles, thus the reported values do not have a statistical meaning. Interestingly, some Moiré patterns are observed for CS1073 sample (Fig. 2b) due to the superimposition of two particles.[39] We couldn't find the Al_2O_3 from HRTEM images that might be due to the existence of a surface over layer of ceria on the alumina support.

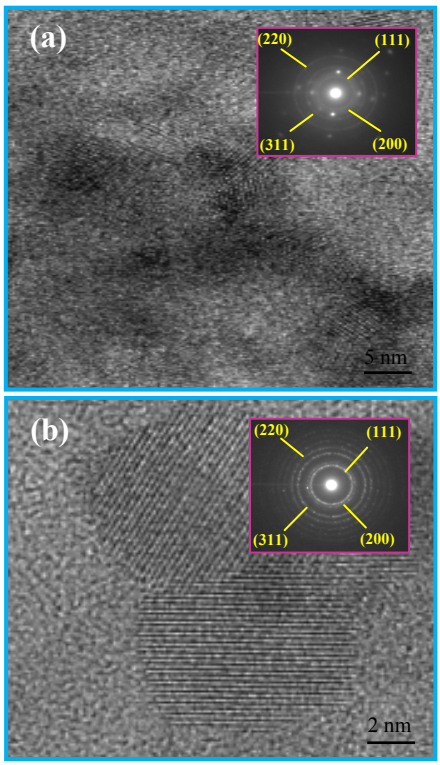

Fig. 3 HRTEM images and the corresponding selected-area electron diffraction (SAED) patterns of CeO_2-Sm_2O_3/Al_2O_3 sample (CSA) calcined at (a) 773 K and (b) 1073 K.

TG-DTA profiles of oven-dried Ce-Sm and Ce-Sm/Al_2O_3 samples showed an exothermic weight loss peak in the range of 373–423 K, which can be assigned to desorption of water molecules (Fig. S1, ESI †).[22] Additionally, a weight loss peak was found at ~573 K for the Ce-Sm/Al_2O_3 sample attributed to desorption of the carbonate species. On the other hand, the Ce-Sm sample showed a weight loss peak at higher temperatures (~863 K), which indicates desorption of hydroxycarbonate and/or polycarbonate species.[28,40] The presence of hydroxyl and carbonate groups on the catalyst surface is due to unique acidic- and basic-properties of ceria.[28] Although we used metal nitrates as the precursors, no peaks corresponding to decomposition of nitrates were observed. The thorough washing procedure of the samples with the double distilled water is the main reason for this observation. The elemental analysis of the samples was performed using ICP-OES technique. The atomic ratio of Ce/Sm in the CeO_2-Sm_2O_3 and CeO_2-Sm_2O_3/Al_2O_3 was found to be ~61/39 and 62/38, which are very close to the expected values (Ce/Sm = 60/40).

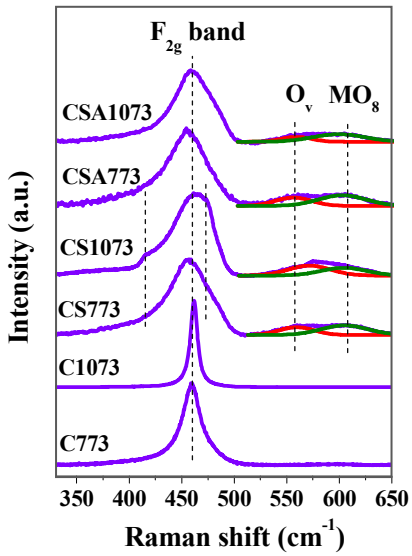

Fig. 4 Raman spectra of pure CeO_2 (C), CeO_2-Sm_2O_3 (CS) and CeO_2-Sm_2O_3/Al_2O_3 (CSA) samples calcined at 773 and 1073 K. O_v – oxygen vacancy band and MO_8 – SmO_8-type complex band.

Raman spectroscopy analysis was carried out to examine the structural properties of the CeO_2 modified by the addition of dopant (Sm) and the support (Al_2O_3). Fig. 4 shows the visible Raman spectra of the Ce-Sm and Ce-Sm/Al_2O_3 samples, along with pure CeO_2. The observed sharp peak at ~460 cm^{-1} in pure CeO_2 can be assigned to F_{2g} mode due to symmetrical stretching of Ce-O vibrational unit in fluorite-type CeO_8 structure.[28] Interestingly, the F_{2g} band of Ce-Sm and Ce-Sm/Al_2O_3 samples was broadened and shifted to various extents with respect to pristine CeO_2 (Table 2). These observations could be attributed to several factors, including phonon confinement, lattice strain, inhomogeneity of the size distribution, lattice defects, and variation in the phonon relaxation with the particle size.[41] Furthermore, no Sm_2O_3 Raman bands (cubic Sm_2O_3 ~375 cm^{-1}) were identified in both Ce-Sm and Ce-Sm/Al_2O_3 samples, which indicate incorporation of Sm into the CeO_2 lattice, and corroborating the XRD results very well. In addition to F_{2g} band, two Raman bands at about 560 and 610 cm^{-1} were found in Ce-Sm and Ce-Sm/Al_2O_3 samples. The observed Raman band at ~560 cm^{-1} can be assigned to defect-induced mode arising due to

the presence of oxygen vacancies (O_v) in the ceria lattice.[42-44] The variation in the oxidation states of dopant (Sm^{3+}) and host (Ce^{4+}) is responsible for the formation of oxygen vacancies in the synthesized samples. Appearance of another Raman band at ~610 cm^{-1} indicates stretching vibration of defective SmO_8-type complex, which is due to disparity in the ionic radii of the Sm^{3+} (1.08 Å) and Ce^{4+} (0.97 Å). This band represents defect species with O_h symmetry associated with dopant cation in 8-fold coordination of O^{2-}.[42-44] It has been demonstrated that SmO_8 complex band does not contain any oxygen species. Moreover, two additional weak bands at ~415 and 474 cm^{-1} are noticed in the CS sample calcined at 1073 K, attributed to distortion in the ceria lattice.[45] On the other hand, no Raman bands pertaining to the Al_2O_3 were found for all CSA samples, which is due to its strong Raman background in the visible and near IR region.[46]

Table 2 Position of F_{2g} peak, its full width at half maxima (FWHM), and intensity ratio of the O_v band to the F_{2g} band (I_{Ov}/I_{F2g}) of pure CeO_2 (C), CeO_2-Sm_2O_3 (CS), and CeO_2-Sm_2O_3/Al_2O_3 (CSA) samples calcined at different temperatures

Sample	F_{2g} peak (cm^{-1})[a]	FWHM of F_{2g} peak[a]	I_{OV}/I_{F2g}[a]
C773	460.6	30.24	-
C1073	462.1	8.52	-
CS773	455.9	51.55	0.0951
CS1073	459.6	48.54	0.0822
CSA773	452.3	52.74	0.0928
CSA1073	458.4	47.32	0.0663

[a] From Raman spectra.

It is interesting to note from Fig. 4 that the intensity of the SmO_8-type complex band decreases with the increase of calcination temperature for all samples, attributed to the reduction of its defective nature.[42-44] This unusual observation reveals the formation of perfect crystal lattice at higher calcination conditions due to well ordering level of the samples. On the other hand, the intensity ratio of the O_v band to the F_{2g} band (I_{Ov}/I_{F2g}) is estimated to know the concentration of oxygen vacancies present in the CeO_2-based solid solutions in such a way that a higher ratio indicates a higher oxygen vacancy concentration (Table 2). It was found that unsupported Ce-Sm sample shows a slightly higher amount of oxygen vacancies compared with Ce-Sm/Al_2O_3 sample. Surprisingly, with the increase of calcination temperature the concentration of oxygen vacancies was drastically decreased, and this effect is highly pronounced in the case of Ce-Sm/Al_2O_3 sample. This observation is due to the migration of bulk Sm^{3+} ions into the catalyst surface (evidenced from XPS studies), hence reduction of the bulk oxygen vacancies. Moreover, no oxygen vacancies were noticed for CeO_2 calcined at 773 and 1073 K, which indicates the importance of dopant in the enhancement of oxygen vacancies of the CeO_2.

XPS measurements were performed to know the oxidation states of the elements as well as to estimate the Ce/Sm atomic ratio in the Ce-Sm samples. The obtained electron binding energy (BE) values are summarized in Table 3. Fig. 5 shows the Ce 3d core level spectra of the CeO_2, Ce-Sm, and Ce-Sm/Al_2O_3 samples. Usually, the ceria-based materials exhibit a complex Ce 3d XP spectrum due to hybridization of Ce 4f with ligand orbitals and fractional occupancy of the valence 4f orbitals.[47] In addition to the spin-orbit splitting of the Ce $3d_{5/2}$ and Ce $3d_{3/2}$, several other splittings are also possible due to a redistribution of the entire energy spectrum when a core hole is generated.[48] Fujimori et al. have discussed this phenomenon in detail and it is not our intention to examine it further here.[49-51] As shown in the Fig. 5, the Ce 3d spectra are composed of ten peaks, represented by u and v labels, corresponding to Ce $3d_{3/2}$ and Ce $3d_{5/2}$, respectively. Amongst, six peaks (v, v'', v''', u, u'', and u''') indicate three pairs of spin-orbit doublets of Ce^{4+}, whereas four peaks (v_0, v', u_0, and u') signify two pairs of Ce^{3+}.[28] These findings clearly reveal the presence of both Ce^{3+} and Ce^{4+} ions in the ceria-based materials. It can be seen from Fig. 5 that the intensity of the u''' peak (a qualitative fingerprint of Ce^{4+} ions) was increased for Ce-Sm and Ce-Sm/Al_2O_3 samples.[52,53] This observation indicates the presence of small amounts of Ce^{3+} ions over the surface of Ce-Sm and Ce-Sm/Al_2O_3 samples attributed to their different reducible nature induced by Sm^{3+} ions present on the catalyst surface.

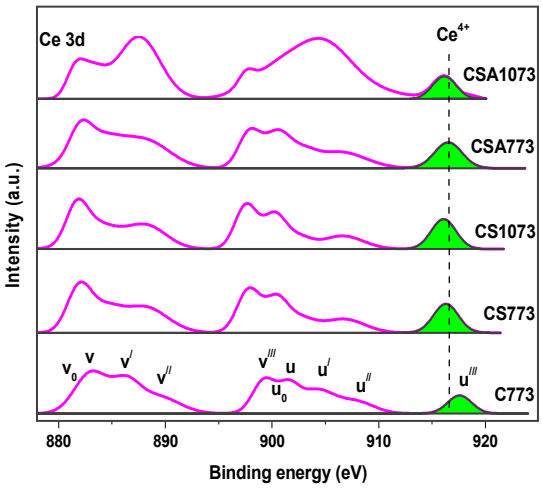

Fig. 5 Ce 3d XP spectra of pure CeO_2 (C), CeO_2-Sm_2O_3 (CS) and CeO_2-Sm_2O_3/Al_2O_3 (CSA) samples.

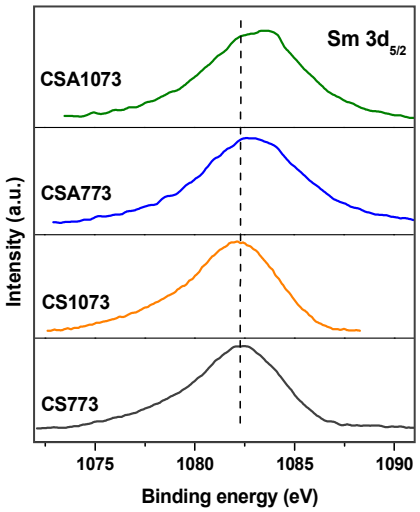

Fig. 6 Sm $3d_{5/2}$ XP spectra of Ce-Sm (CS) and Ce-Sm/Al_2O_3 (CSA) samples calcined at different temperatures.

Fig. 6 shows Sm $3d_{5/2}$ core level spectra of the Ce-Sm and Ce-Sm/Al_2O_3 samples calcined at 773 and 1073 K. A major band was identified in the range of ~1082.1–1083.2 eV, which indicates the presence of Sm^{3+} in Ce-Sm samples.[54] It is interesting to note from Table 3 that the addition of Al_2O_3 to Ce-Sm sample increases the BE value of Sm $3d_{5/2}$, revealing the influence of the Al_2O_3 on the chemical environment of Sm in the Ce-Sm/Al_2O_3 sample

Table 3 XPS core level binding energies of Ce $3d_{3/2}$, Sm $3d_{5/2}$, Al 2p and O 1s as well as Ce/Sm ratio of pure CeO_2, Ce-Sm, and Ce-Sm/Al_2O_3 samples

Sample	Ce $3d_{3/2}$, u''' (eV)	Sm $3d_{5/2}$ (eV)	O 1s (eV)	Al 2p (eV)	Ce/Sm ratio
C773	917.3	–	528.8	–	–
CS773	916.2	1082.3	528.9	–	5.8
CS1073	916.0	1082.1	528.7	–	5.1
CSA773	916.4	1082.8	531.5	74.1	5.5
CSA1073	916.1	1083.2	531.4	74.4	4.7

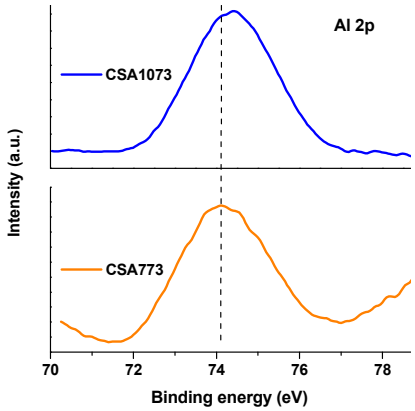

Fig. 7 Al 2p XP spectra of Ce-Sm/Al_2O_3 (CSA) sample calcined at 773 and 1073 K.

The Al 2p XP spectra of Ce-Sm/Al_2O_3 sample calcined at different temperatures are shown in Fig. 7. The observed slight increase in the BE value of the CSA1073 sample (74.4 eV) compared with that of the CSA773 sample (74.1 eV) might be due to the disappearance of the surface hydroxyl groups present on the Al_2O_3 support. Upon thermal treatment, water is normally released from two neighbouring hydroxyl ions that leave the coordination sphere of an aluminum ion incomplete.[55] Consequently, the reduction of negative charge density from the alumina center can be expected, which is reflected in the estimated binding energy.

Fig. 8 represents the O 1s XPS core-level spectra of Ce-Sm and Ce-Sm/Al_2O_3 samples. Obviously, the ceria-based catalysts show more than one type of oxygen ions. A main peak at 528.5±0.3 eV was noticed for the Ce-Sm sample that can be assigned to the lattice oxygen of ceria.[56] Appearance of another peak at 531.0±0.3 eV indicates existence of various hydroxyl and/or carbonyl groups on the catalyst surface, which are further confirmed by FTIR study (Fig. S2, ESI†).[12,28,47] The lattice oxygen peak position and its broadness of pure ceria are considerably different compared with that of the Ce-Sm and Ce-Sm/Al_2O_3 samples, which is might due to variation in the chemical environment of the Ce-O bond after the addition of dopant (Sm) to the ceria (Fig. S3, ESI†). Interestingly, shifting of O 1s peaks towards higher binding energies was found in the Ce-Sm/Al_2O_3 sample (Table 3). In the case of Al_2O_3 supported Ce-Sm samples, an additional peak can be observed at 533.2±0.4 attributed to the presence of Al-O bond.[27]

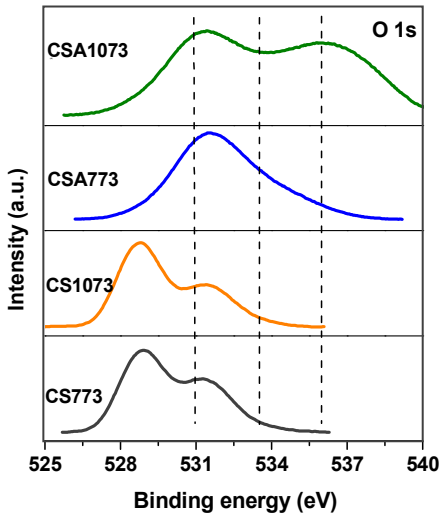

Fig. 8 O 1s XP spectra of Ce-Sm (CS) and Ce-Sm/Al_2O_3 (CSA) samples calcined at different temperatures.

Table 3 shows the Ce/Sm atomic ratio of the Ce-Sm and Ce-Sm/Al_2O_3 samples estimated by XPS analysis. It was found that the calculated Ce/Sm atomic ratio for both samples largely deviates from the expected value (Ce/Sm = 60/40). Two possible mechanisms, i.e., Ce-segregation at the surface and/or Sm-enrichment associated with oxygen vacancies in the bulk are responsible for the decreased atomic ratio. Further, with the increase of calcination temperature from 773 to 1073 K, a decrease in the Ce/Sm atomic ratio was noted, suggesting the diffusion of bulk Sm^{3+} cations to the catalyst surface at higher thermal treatments. Amongst, the CSA1073 sample has lowest Ce/Sm atomic ratio. Therefore, a reduction in the bulk oxygen vacancies can be expected at higher temperature calcined samples, in good agreement with the Raman studies (Table 2).

Crystalline ceria has a band gap of 3.1 eV and absorbs strongly in the UV region with absorption threshold near 400 nm due to charge-transfer transitions between O 2p and Ce 4f bonds.[57] Fig. 9 displays the UV-vis DRS spectra of Ce-Sm and Ce-Sm/Al_2O_3 samples. All samples exhibit two absorption maxima in UV region entered at ~255 and 336 nm, which indicates $O^{2-} \rightarrow Ce^{3+}$ and inter-band transitions, respectively.[12] The observed weak bands between 450 and 650 nm particularly in CS1073 indicates surface $Ce^{3+} \rightarrow Ce^{4+}$ transitions.[58]

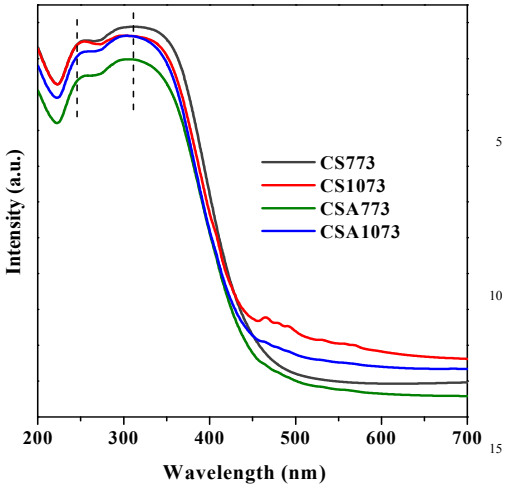

Fig. 9 UV-vis DRS studies of CeO_2-Sm_2O_3 (CS) and CeO_2-Sm_2O_3/Al_2O_3 (CSA) samples calcined at different temperatures.

3.2. Soot oxidation activity studies

The soot oxidation measurements were performed in 'tight contact' mode with catalyst-soot mixtures in 4:1 wt/wt ratio. Printex-U is used as the model soot in the present work. The normalized soot conversion as a function of temperature over pure CeO_2, Ce-Sm, and Ce-Sm/Al_2O_3 samples is presented in Fig. 10. For comparison, un-catalyzed soot oxidation is also included. As can be noted from the figure, both Ce-Sm and Ce-Sm/Al_2O_3 catalysts show a decreased soot oxidation temperature. A sharp increase of soot conversion for both Ce-Sm and Ce-Sm/Al_2O_3 samples is observed after 678 and 681 K of reaction temperature, respectively. For better comparison of the activities, we highlighted the T_{50} values, temperature at which 50% soot conversion was achieved, of the investigated samples.[54] The estimated T_{50} values for pristine CeO_2, Ce-Sm and Ce-Sm/Al_2O_3 samples calcined at 773 K are ~835, 690 and 697 K, respectively. On the other hand, under uncatalyzed conditions, the soot conversion is very low (i.e., T_{50} ~880 K). This interesting observation clearly indicates the necessity of the ceria-based materials for the diesel soot oxidation.

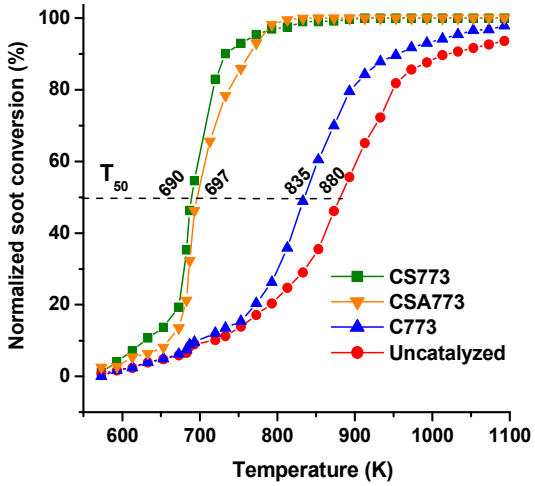

Fig. 10 Normalized soot conversion (%) versus reaction temperature (K) of bare soot, pure CeO_2 (C), Ce-Sm (CS), and Ce-Sm/Al_2O_3 (CSA) samples calcined at 773 K.

Fig. 11 shows the normalized soot oxidation profiles of Ce-Sm and Ce-Sm/Al_2O_3 samples calcined at 1073 K. The 50% soot conversion was found to be at ~728 and 744 K for Ce-Sm and Ce-Sm/Al_2O_3 samples. Evidently, the difference between the T_{50} values of the 1073 calcined Ce-Sm and Ce-Sm/Al_2O_3 samples is more when compared with that of the 773 calcined Ce-Sm and Ce-Sm/Al_2O_3 samples. Liu *et al.* investigated the catalytic performance of Ce-Sm mixed oxides for the soot oxidation under loose contact mode with 10:1 ratio of catalyst and soot.[7] It was reported that doped CeO_2 exhibits low soot oxidation efficiency compared with bare CeO_2. In contrast, the Ce-Sm and Ce-Sm/Al_2O_3 samples showed better soot oxidation performance in comparison to CeO_2 in the present study. However, it must be understand here that the direct comparison of Liu *et al*. results with our results is rather difficult due to the different preparation method employed and the reaction conditions applied, as well as due to different doping amounts of the Sm-oxide.

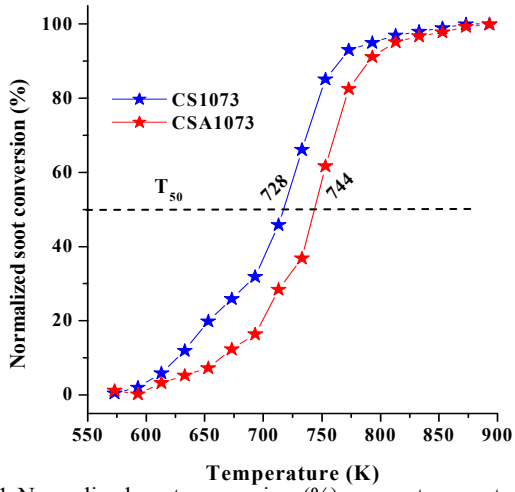

Fig. 11 Normalized soot conversion (%) versus temperature (K) of Ce-Sm (CS) and Ce-Sm/Al_2O_3 (CSA) samples calcined at 1073 K.

The catalytic performance of ceria-based materials, especially for soot oxidation depends on several factors, including particle size, BET surface area, lattice oxygen mobility, oxygen vacancies, active oxygen formation, etc.[7,12,13] Particularly, when the particle size is reduced to nanoscale, the density of defect sites and/or the number of unsaturated coordinated sites largely increases, which could play a key role in gas-solid catalysis.[7] It was shown that a decrease in the particle size from 1 μm to 10 nm will increase the contact of soot and catalyst by 100 times.[7] As well, the performance of a catalyst is closely related to its surface area. However, in the present study no clear correlation was found between the activity results and the crystallite size as well as surface area of the investigated samples (evidence from Table 1 and Fig. 10). Despite its low surface area, the Ce-Sm sample exhibited better catalytic performance compared with Ce-Sm/Al_2O_3 sample (Fig. 10). It must be emphasized here that the dependence of the performance of ceria-based materials in soot oxidation is insignificant when the surface area is above a value of ca. 40 m^2/g.[13] Therefore, it can be suggested that BET surface area is not the only parameter to explain the soot combustion performance of the ceria-based catalysts.[60]

It has been demonstrated that the active oxygen species present on the surface of ceria-based catalysts plays a favourable role in the soot oxidation.[1,12,13] Usually, the active oxygen can be created by adsorption of gaseous oxygen on the oxygen vacancies of ceria as shown in Fig. 12. This active oxygen spillover to the soot adsorbed on the catalyst surface, leading to the formation of CO_x species. The generated vacancy will be eventually refilled by lattice oxygen of CeO_2. Therefore, the high soot oxidation performance of Ce-Sm and Ce-Sm/Al_2O_3 samples compared with pure CeO_2 is attributed to the presence of large amount of oxygen vacancies (Table 2). Raman studies clearly revealed that the Ce-Sm sample exhibits more number of oxygen vacancies compared with Ce-Sm/Al_2O_3 sample. Hence, it can be suggested that the Ce-Sm sample has strong ability to form more active oxygen species compared with Ce-Sm/Al_2O_3 sample, and thereby, high soot oxidation activity (Figs. 10 and 11). It was reported that perfect stoichiometry of the CeO_2 contains small concentration of oxygen vacancies.[61] It is expected that the addition of Al_2O_3 to the Ce-Sm mixed oxide enhances its structural stability through Ce-O-Al interactions at the boundary of the Ce-Sm and Al_2O_3, and consequently, small amounts of oxygen vacancies and low soot oxidation performance. A clear explanation can be found from the density functional theory analysis of doped CeO_2 materials, which is under further investigation.[60] Although no oxygen vacancies were found in the pure CeO_2 (Fig. 4), its soot oxidation efficiency could be attributed to generation of oxygen vacancies under reaction conditions, followed by rapid and repeatable redox cycles of Ce^{4+}/Ce^{3+}.[62-64] Despite its slightly low catalytic performance compared with Ce-Sm sample, the superior thermal stability of the Ce-Sm/Al_2O_3 sample is crucial in view of the practical working conditions of the diesel engines.

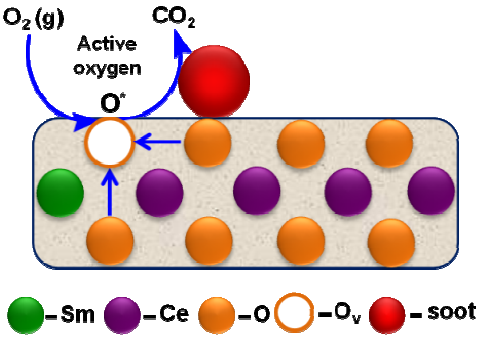

Fig. 12 Probable mechanism for soot oxidation over Ce-Sm solid solution.

Fig. 13 shows the correlation of 50% soot oxidation performance (T_{50} values) of the Ce-Sm and Ce-Sm/Al_2O_3 samples with that of Ce-Pr,[65] Ce-La,[12] and Ce-Zr[12] catalysts prepared by similar preparation method. It is evident from Fig. 13 that the Ce-Sm and Ce-Sm/Al_2O_3 samples exhibit 50% soot conversion at much lower temperatures compared with other doped ceria catalysts. The high soot oxidation performance of the Ce-Sm nano-oxides is due to strong synergetic effect between the Ce and Sm in the Ce-Sm and Ce-Sm/Al_2O_3 catalysts.

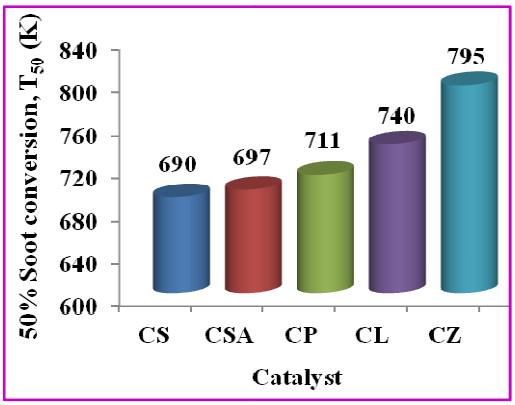

Fig. 13 Correlation of soot oxidation performance (T_{50} values) of Ce-Sm (CS), Ce-Sm/Al_2O_3 (CSA), Ce-Pr (CP), Ce-La (CL), and Ce-Zr (CZ) samples calcined at 773 K.

4. Conclusions

Nanosized Ce-Sm and Ce-Sm/Al_2O_3 solid solutions were successfully prepared by coprecipitation and deposition coprecipitation methods, respectively. Their physicochemical properties were deeply investigated by means of various spectroscopic and non-spectroscopic techniques. The XRD studies clearly showed the formation of nanocrystalline single phase Ce-Sm-O solid solutions. It was found that the addition of Sm and Al_2O_3 to CeO_2 significantly reduces its crystallite size, and thereby improved BET surface area. Raman studies revealed the presence of large amount of oxygen vacancies in the Ce-Sm and Ce-Sm/Al_2O_3 samples compared with pure CeO_2. However, the oxygen vacancy concentration was considerably decreased at higher calcination temperatures attributed to diffusion of the bulk Sm^{3+} to the catalyst surface. Activity results revealed that both Ce-Sm and Ce-Sm/Al_2O_3 catalysts show better soot oxidation performance in comparison to pure CeO_2. The 50% soot conversion for Ce-Sm, Ce-Sm/Al_2O_3 and pure CeO_2 samples was found to be ~690, 697 and 835 K, respectively. The presence of abundant oxygen vacancies associated with smaller crystallite size and superior BET surface area are attributed to outstanding activity of the Ce-Sm and Ce-Sm/Al_2O_3 samples.

Acknowledgments

P.S. and K.K. thank the Council of Scientific and Industrial Research (CSIR), New Delhi for senior research fellowships. Financial support was received from Department of Science and Technology, New Delhi, under SERB Scheme (SB/S1/PC-106/2012).

References

1 P. A. Kumar, M. D. Tanwar, S. Bensaid, N. Russo and D. Fino, *Chem. Eng. J.*, 2012, **207–208**, 258–266.
2 K. N. Rao, P. Venkataswamy and B. M. Reddy, *Ind. Eng. Chem. Res.*, 2011, **50**, 11960–11969.
3 R. Zhang, N. Luo, B. Chen and S. Kaliaguine, *Energ. Fuel.*, 2010, **24**, 3719–3726.
4 A. Mishra and R. Prasad, *Catal. Rev. -Sci. Eng.*, 2014, **56**, 57–

81.
5 Y. Wei, J. Liu, Z. Zhao, A. Duan and G. Jiang, *J. Catal.,* 2012, **287**, 13–29.
6 E. Aneggi, C. de Leitenburg, G. Dolcetti and A. Trovarelli, *Catal. Today,* 2008, **136**, 3–10.
7 J. Liu, Z. Zhao, Y. Chen, C. Xu, A. Duan and G. Jiang, *Catal. Today,* 2011, **175**, 117–123.
8 Q. Wang, J. S. Chung and Z. Guo, *Ind. Eng. Chem. Res.,* 2011, **50**, 8384–8388.
9 J. Liu, Z. Zhao, J. Xu, C. Xu, A. Duan, G. Jianga and H. He, *Chem. Commun.,* 2011, **47**, 11119–11121.
10 Y. Wei, J. Liu, Z. Zhao, Y. Chen, C. Xu, A. Duan, G. Jiang and H. He, *Angew. Chem.,* 2011, **123**, 2374–2377.
11 A. M. Hernández-Giménez, L. P. dos Santos Xavier and A. Bueno-López, *Appl. Catal. A: Gen.,* 2013, **462–463**, 100–106.
12 L. Katta, P. Sudarsanam, G. Thrimurthulu and B. M. Reddy, *Appl. Catal. B: Environ.,* 2010, **101**, 101–108.
13 E. Aneggi, C. de Leitenburg and A. Trovarelli, *Catal. Today,* 2012, **181**, 108–115.
14 J. Paier, C. Penschke and J. Sauer, *Chem. Rev.,* 2013, **113**, 3949−3985.
15 W. C. Chueh, C. Falter, M. Abbott, D. Scipio, P. Furler, S. M. Haile and A. Steinfeld, *Science,* 2010, **330**, 1797–1801.
16 H. Li, G. Wang, F. Zhang, Y. Cai, Y. Wang and I. Djerdj, *RSC Adv.,* 2012, **2**, 12413–12423
17 N. K. V. Leitner, F. Delanoë, B. Acedo and B. Legube, *New J. Chem.,* 2000, **24,** 229–233.
18 N. Imanaka, T. Masui, T. Egawa and H. Imadzu, *J. Mater. Chem.,* 2009, **19**, 208–210.
19 R. Farra, M. García-Melchor, M. Eichelbaum, M. Hashagen, W. Frandsen, J. Allan, F. Girgsdies, L. Szentmiklósi, N. López and D. Teschner, *ACS Catal.,* 2013, **3**, 2256−2268.
20 R. B. Duarte, S. Damyanova, D. C. de Oliveira, C. M. P. Marques and J. M. C. Bueno, *Appl. Catal. A: Gen.,* 2011, **399**, 134–145.
21 R. B. Duarte, M. Nachtegaal, J. M. C. Bueno and J. A. van Bokhoven, *J. Catal.,* 2012, **296**, 86–98.
22 K. Kuntaiah, P. Sudarsanam, B. M. Reddy and Ajayan Vinu, *RSC Adv.,* 2013, **3**, 7953–7962
23 Y. Dong, D. Li, X. Feng, X. Dong and S. Hampshire, *RSC Adv.,* 2013, **3**, 17395–17401.
24 R. T. Baker, L. M. Gomez-Sainero and I. S. Metcalfe, *J. Phys. Chem. C,* 2009, **113**, 12465–12475.
25 N. Sutradhar, A. Sinhamahapatra, S. Pahari, M. Jayachandran, B. Subramanian, H. C. Bajaj and A. B. Panda, *J. Phys. Chem. C,* 2011, **115**, 7628–7637.
26 S. Mandal, K. K. Bando, C. Santra, S. Maity, O. O. James, D. Mehtad and B. Chowdhury, *Appl. Catal. A: Gen.,* 2013, **452**, 94–104.
27 L. Katta, G. Thrimurthulu, B. M. Reddy, M. Muhler and W. Grunert, *Catal. Sci. Technol.,* 2011, **1**, 1645–1652.
28 P. Sudarsanam, B. Mallesham, P. S. Reddy, D. Großmann, W. Grünert and B. M. Reddy, *Appl. Catal. B: Environ.,* 2014, **144**, 900–908.
29 Y. J. Kim, Y. S. Kim, S. Y. Chai, D. H. Cha, Y. S. Choi and W. I. Lee, *New J. Chem.,* 2007, **31**, 260−264.
30 X. Wu, S. Liu, D. Weng, F. Lin and R. Ran, *J. Hazard. Mater.,* 2011, **187**, 283–290.
31 B. M. Reddy, K. N. Rao and P. Bharali, *Ind. Eng. Chem. Res.,* 2009, **48**, 8478–8486.
32 S. Cava, S. M. Tebcherani, I. A. Souza, S. A. Pianaro, C. A. Paskocimas, E. Longob and J. A. Varela, *Mater. Chem. Phys.,* 2007, **103**, 394–399.
33 Q. Dong, S. Yin, C. Guo and T. Sato, *Nanoscale Res. Lett.,* 2012, **7**, 542–546.
34 N. S. Priya, C. Somayaji and S. Kanagaraj, *J. Nanopart. Res.,* 2014, **16**, 2214–2223.
35 B. M. Reddy, K. N. Rao, G. K. Reddy, A. Khan and S. -E. Park, *J. Phys. Chem. C,* 2007, **111**, 18751−18758.
36 M. Fernandez-Garcıa, A. Martınez-Arias, J. C. Hanson and J. A. Rodriguez, *Chem. Rev.,* 2004, **104**, 4063−4104.
37 B. Bonnetot, V. Rakic, T. Yuzhakova, C. Guimon and A. Auroux, *Chem. Mater.,* 2008, **20**, 1585–1596.
38 D. Zhang, X. Du, L. Shia and R. Gao, *Dalton Trans.,* 2012, **41**, 14455–14475.
39 F. Yang, J. Graciani, J. Evans, P. Liu, J. Hrbek, J. F. Sanz and J. A. Rodriguez, *J. Am. Chem. Soc.,* 2011, **133**, 3444–3451.
40 B. Azambre, S. Collura, P. Darcy, J. M. Trichard, P. Da Costa, A. García-García and A. Bueno-López, *Fuel Process. Technol.,* 2011, **92**, 363–371.
41 B. M. Reddy, G. Thrimurthulu and L. Katta, Y. Yamada, S.-E. Park, *J. Phys. Chem. C,* 2009, **113**, 15882–15890.
42 L. Li, F. Chen, J.-Q. Lu and M.-F. Luo, *J. Phys. Chem. A,* 2011, **115**, 7972–7977.
43 T. Taniguchi, T. Watanabe, N. Sugiyama, A. K. Subramani, H. Wagata, N. Matsushita and M. Yoshimura, *J. Phys. Chem. C,* 2009, **113**, 19789–19793.
44 M. H. Zoellner, G. Niu, J.-H. Jhang, A. Schaefer, P. Zaumseil, M. Baumer and T. Schroeder, *J. Phys. Chem. C,* 2013, **117**, 24851−24857.
45 S. Agarwal, X. Zhu, E. J. M. Hensen, L. Lefferts and B. L. Mojet, *J. Phys. Chem. C,* 2014, **118**, 4131−4142.
46 H. Kim, K. M. Kosuda, R. P. Van Duynea and P. C. Stair, *Chem. Soc. Rev.,* 2010, **39**, 4820−4844.
47 P. Sudarsanam, L. Katta, G. Thrimurthulu and B. M. Reddy, *J. Ind. Eng. Chem.,* 2013, 19, 1517–1524.
48 N. Acerbi, S. Golunski, S. C. Tsang, H. Daly, C. Hardacre, R. Smith and P. Collier, *J. Phys. Chem. C,* 2012, **116**, 13569−13583.
49 A. Fujimori, *Phys. Rev. B,* 1983, **27**, 3992−4001.
50 A. Fujimori, *Phys. Rev. B,* 1983, **28**, 2281−2283.
51 A. Fujimori, *Phys. Rev. B,* 1983, **28**, 4489−4499.
52 Y. Wang, Z. Quan and J. Lin, *Inorg. Chem.,* 2007**, 46**, 5237−5242.
53 Z. L. Wang, G. R. Li, Y. N. Ou, Z. P. Feng, D. L. Qu and Y. X. Tong, *J. Phys. Chem. C,* 2011, **115**, 351–356.
54 L. M. Gomez-Sainero, R. T. Baker, I. S. Metcalfe, M. Sahibzada, P. Concepcione and J. M. Lopez-Nieto, *Appl. Catal. A: Gen.,* 2005, **294**, 177–187
55 B. M. Reddy, B. Chowdhury, E. P. Reddy and A. Fernández *Appl. Catal. A: Gen.,* 2001, 213, 279–288.
56 P. Sudarsanam, B. Mallesham, D. N. Durgasri and B. M. Reddy, *J. Ind. Eng. Chem.,* 2014, **20**, 3115–3121.
57 L. Katta, P. Sudarsanam, B. Mallesham and B. M. Reddy, *Catal. Sci. Technol.,* 2012, **2**, 995–1004.
58 G. R. Rao and H. R. Sahu, Proc. *Indian Acad. Sci. (Chem.*

Sci.), 2001, **113**, 651–658.
59 E. Aneggi, D. Wiater, C. de Leitenburg, J. Llorca and A. Trovarelli, *ACS Catal.,* 2014, **4**, 172−181.
60 N. Guillén-Hurtado, A. Bueno-López and A. García-García, *Appl. Catal. A: Gen.,* 2012, **437–438**, 166–172.
61 M. Nolan, Y. Lykhach, N. Tsud, T. Skala, T. Staudt, K. C. Prince, V. Matolın and J. Libuda, *Phys. Chem. Chem. Phys.,* 2012, **14**, 1293–1301.
62 P. Sudarsanam, B. Mallesham, D. N. Durgasri and B. M. Reddy, *RSC Adv.,* 2014, **4**, 11322–11330
63 M. V. Ganduglia-Pirovano, A. Hofmann and J. Sauer, *Surf. Sci. Rep.,* 2007, **62**, 219–270.
64 W. Y. Hernandez, M. A. Centeno, F. Romero-Sarria and J. A. Odriozola, *J. Phys. Chem. C,* 2009, **113**, 5629–5635.
65 G Thrimurthulu, K. N. Rao, D. Devaiah and B. M. Reddy, *Res. Chem. Intermediate.,* 2012, **38**, 1847–1855.